J. Fluid Mech. (1994), *vol.* 271, *pp.* 153–172

Experiments on spin-up and spin-down on a β-plane

By W. J. JILLIANS AND T. MAXWORTHY

Department of Aerospace Engineering, University of Southern California, Los Angeles, CA 90089-1191, USA

(Received 4 March 1992 and in revised form 21 January 1994)

Here we study the spin-up and spin-down of a homogeneous fluid with a free surface on an experimental 'β-plane' and describe the important features for both cases over a range of parameters. Quantitative values are found for the velocity fields using a new image processing technique that analyses a video record of particle motion and stores the results digitally. Streamlines, pressure fields and vorticity values are found by interpolation techniques and result in a complete description of the flow characteristics. We discuss the relationship between the results of these experiments and those observed in large-scale homogeneous models of ocean circulation, e.g. Moore (1963). This study extends the work of van Heijst *et al.* (1990) to the case of spin-up in a rectangular container but of non-uniform depth and we note the differences to and similarities with their observations. It is related, also, to more recent results of Maas *et al.* (1992), who considered spin-up on a β-plane but in a tank of very different proportions to the one considered here.

1. Introduction

Homogeneous models of the wind-driven ocean circulation have been of interest since Stommel (1948) formulated his simplified model of large-scale homogeneous ocean dynamics. It is now realized that a model incorporating all the observed physical mechanisms may be too complicated to be gainfully studied and attention has focused on situations in which simplifying arguments allow the neglect of some physical complexities. Thus, much work has been done to incorporate a selected combination of horizontal and/or vertical friction, steady and unsteady wind stresses, nonlinear-inertial and rotation effects in β-plane models where some dimensionless combinations of these effects can be considered small in order to make the problem analytically tractable.

The first work to discuss the combined importance of friction and inertia in the development of the western boundary current is Moore (1963). He considered a steady wind-driven inertial flow and found solutions to the vorticity equation, with the appropriate boundary conditions asymptotically correct at their outer edge. By considering the purely inertial theory of Fofonoff (1954), it can be shown that the only free mode is a steady east-to-west flow with dissipation of energy in high-speed boundary currents such as the western boundary current. Using an appropriate wind stress to drive the flow, Moore extended this basic model to include frictional wall effects and demonstrated how departures from geostrophy manifest themselves as standing Rossby waves in the region beyond the western boundary layer. These waves are present along the northern wall with amplitude decaying exponentially with distance from the western wall. In particular, Moore pointed to the importance of a

Reynolds number $Re = U^{\frac{3}{2}}/\nu\beta^{\frac{1}{2}}$ that can be used to distinguish flows for which western boundary-layer dissipation is important ($Re \ll 1$) from those in which the Rossby wave regime dominates ($Re \gg 1$). Here U is a characteristic velocity of the flow, ν the horizontal eddy viscosity, $\beta = 2\Omega\cos\theta/R$, Ω is the rotation rate, θ the latitude and R the radius of the sphere on which the motion takes place. Subsequently, Bryan (1963) developed a numerical model that integrated the vorticity equation in a rectangular basin while ignoring bottom friction. Adopting a similar numerical approach, Veronis (1966) looked at a flow which incorporated nonlinear inertial effects and friction. Both numerical models were able to predict the western intensification of the circulation as well as the formation of north–south asymmetry and undulations in the eastward extensions of the western boundary current.

In this paper, we generate an experimental flow that has some striking similarities to these large-scale homogeneous ocean model circulations. We use a large rectangular tank that can be uniformly rotated and that is fitted with an inclined bottom to imitate the β-plane effect. With step forcing, the evolving motion is not steady but consists of a spin-up/down flow that is unsteady as the flow accelerates/decelerates to a stationary state in the new rotating frame of reference.

The dominant physical processes that determine the flow characteristics in this rapidly rotating domain are expressed in the Taylor–Proudman theorem and conservation of potential vorticity. Briefly stated, the horizontal velocity vector is independent of z, so that fluid columns preferentially travel along paths of constant depth unless forced to deviate owing to topographic constraints. When this occurs, relative vorticity of one sign or the other is generated depending on whether the flow experiences a depth change that is deepening (generating relative cyclonic vorticity) or shoaling (generating anticyclonic vorticity).

The first notable theory to employ a topographic β-plane was that of Pedlosky & Greenspan (1967) who used the so-called sliced cylinder – a regular cylinder with a planar sloping bottom – which was rotated uniformly with a surface stress applied by a rigid lid turning at a slightly slower rate than that of the cylinder, thus representing the wind stress in a geophysical application. Subsequent experimental work by Beardsley (1969, 1975 *a*, *b*) developed this approach further and led to a numerical model that could accurately describe the experimental results. Sidewall boundary-layer formation was observed with separation of vortices from the wall and westward propagation of a disturbance in a manner suggestive of Rossby waves. For a full description of spin-up in cylindrical and spherical containers, see the review of Benton & Clark (1974) and the books by Pedlosky (1975) and Greenspan (1968).

Recent work by van Heijst (1989) and van Heijst, Davies & Davis (1990) has highlighted spin-up in rectangular containers and other non-cylindrical planforms of constant depth. These studies have analysed the flows produced in elliptical and rectangular tanks of different aspect ratios (i.e. L/W = length/width) with free and rigid-lid upper boundaries. In general, the flows observed ultimately break up into a sequence of large-scale vortices, whose number and sign can be directly related to the aspect ratio of the tank. The migration of vortices was shown to depend upon the parabolic shape of the free surface in centrifugally balanced motion. More recently, Maas, van Heijst & Williams (1992) have considered spin-up on a topographic β-plane, experimentally and, to some extent, theoretically for tanks of small aspect ratio ($L/W \sim 0.5$), where the length is measured along the contours of constant depth. The note, in particular, that for spin-up at moderately large Rossby numbers, three-dimensional effects are important in determining the initial flow pattern. In our case, we consider

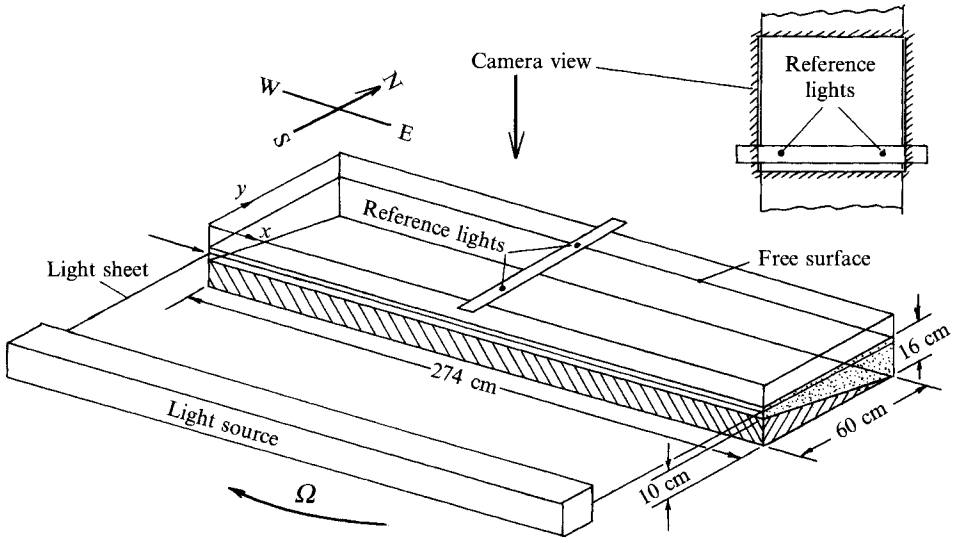

FIGURE 1. Diagram of the experimental apparatus. Also shown is the orientation of the geophysical situation placed above the origin of the tank coordinate system. The field of view of the video camera is shown in the insert.

flow in a tank of large aspect ratio ($L/W = 4.6$) for which such effects do not appear to be of major importance.

One reason why modelling studies of large-scale ocean features have been mostly limited to analytical and numerical methods has been the inability to process large amounts of experimental flow data, from extensive regions and over long time periods, with any accuracy. Recently, however, many advanced techniques have become more affordable for scientific analysis, in particular in the field of image processing using micro-computers. For this reason, we have chosen to implement a new method involving video recording as the medium to collect our data. Previously, particle data have been obtained by photographic means, i.e. taking a single long-time exposure and then digitizing the resulting particle streaks by hand. While data could be accessed laboriously from an extensive region, obtaining a long-time record of such data has proven to be prohibitively time consuming. Here we briefly describe a fully automated method for data acquisition that can capture both a complete continuous record of the flow as well as selected snapshots.

In §2, we describe the experimental apparatus used and the methodology behind the data acquisition. Section 3 then briefly details the Lagrangian particle-image-velocimetry (LPIV) method and the techniques used subsequently to reduce the data and to reconstruct the total velocity field. From the latter, we can derive such flow quantities as vorticity, pressure and streamline patterns.

In §4, we compare the results for the initial velocity field with that found using a simple analytical solution. Other flow features that develop later are presented and a discussion of the physical mechanisms which determine the flow is given. We also examine the effect of varying Rossby number together with the differences between the spin-up and spin-down flow fields. Finally in §5, we discuss the relationship of these results to previous spin-up experiments and to large-scale ocean models.

2. Apparatus

The experimental apparatus consists of a long $490 \times 60 \times 42$ cm^3 transparent Perspex (Lucite) tank mounted on a rotating table (see figure 1). It is free to rotate in either direction and can be turned steadily using a driving motor connected to a simple gearing mechanism so that the speed of rotation can be varied between 1 rev/min (anticlockwise) and 3.5 rev/min (clockwise). Note that we performed this work with the tank rotating in the *clockwise sense* (viewed from above) and so the basic motion is a mirror-image in a plane oriented in the east–west direction of the usual anticlockwise configuration considered in most previous publications. False walls are placed across the tank width to limit the experimental section to 274×60 cm^2 horizontally. An inclined false bottom is also built into the tank so that it lies flush with the real tank bottom at one long side of the tank and rises to 10 cm above the bottom on the opposite side. This design simulates the planetary β-effect with an effective value of $\beta = (2\Omega/h)\,\mathrm{d}h/\mathrm{d}y$, where $h = h_0 + \alpha y$ is the fluid depth, y the north–south coordinate moving down the depth gradient, h_0 is the depth at the shallow 'southern' wall and α the bottom slope, equal to $\frac{1}{6}$ in this case.

A video camera (a Super-VHS portable unit with a built-in VCR) is mounted on a small movable trolley which can be secured at any location along a rail assembly, 1.2 m above the free surface of the test fluid, that runs the length of the tank. To illuminate the flow, an array of arc-lamps is mounted onto the side of the tank to direct a light sheet through the transparent wall and highlight the flow-marking particles. The opposite wall is covered with black masking paper to reduce the reflected glare from the lucite side, an effect that can degrade the particle images by reducing contrast between the particles and their dark background. The arc-lamp array is fitted with a narrow slit in order to illuminate only a thin (1–2 cm) two-dimensional light slice at the level we wish to study, and so contrast is enhanced between particles and the blackened tank walls and bottom.

To provide flow visualization, we introduce white polystyrene particles, of mean diameter 0.6–1.0 mm, liberally into the fluid. Since they have a density slightly greater than water (~ 1.035 g cm^{-3}), salt is added to the water until the majority of particles are neutrally buoyant. We place two small-point light sources a known distance apart on an assembly mounted firmly across the tank. These lights are used as reference points to eliminate camera jitter by allowing us to reposition the digitized frame when analysing the video images. Before the start of an experiment, a reference grid, marked in 5 cm squares, is placed in the camera field of view so as to lie horizontally and at the level of the light sheet. Pictures of this grid are taken while the apparatus is stationary to record a control frame against which to calibrate the experimental data. The tank is then rotated at a uniform angular velocity for 60–90 min in order to ensure that residual motion in the tank has decayed and that the fluid is rotating as a solid body when the experiment is started. To start an experiment, the speed of tank rotation is adjusted to a somewhat higher or lower rate depending on whether we wish to study spin-up or spin-down. The adjustment is made smoothly over a 2–3 s interval to minimize generation of surface waves. We assign the end of this adjustment time as $t = 0$ and refer to it as the 'start-up' in the following description. The video recording is begun slightly before start-up so that we have a record of whatever background residual motion may be present, together with the experimental record that follows (residual velocities are randomly distributed and rarely greater than 0.3 cm s^{-1}).

Preliminary tests with various video camera positions showed that viewing large regions of the tank by placing the camera high above the water surface ($\sim$ 2–3 m) was

possible but reduced the picture resolution and the number of particles that could be successfully identified, thus leading to large velocity errors. For this reason, we decided to keep the camera closer to the surface (~ 1.2 m) so that the video frame completely covered the tank width (see figure 1 for a diagram of the video field), and then to relocate the camera at different positions along the tank length. In this way, by repeating a nominally identical experiment for each camera position, the data can be pieced together by computer after the numerical reduction of the results. With more video cameras, a complete simultaneous record of the flow could have been made. However, the repeatability of an experiment was found to be within experimental error, and so we felt justified in using a patching procedure with video frames that overlapped slightly. Unfortunately, this method results in apparent spatial discontinuities at the boundaries since there is no way to exactly repeat a run with particles in the same positions. Photographic sections have not been marked on the figures that follow, but each section is approximately 40 cm long in the direction of the tank length, so that we need eight sections to cover the whole tank. The flow in a single section, however, can be taken and analysed as a whole, and this will be done in what follows for flow at the eastern end.

Once the data have been collected on video tape, we proceed to analyse and extract velocity, vorticity and other flow characteristics. The video record is up-loaded onto a high-resolution Sony U-Matic 9600 $\frac{3}{4}$ inch VCR to which we add a serial frame code for accurate identification of each individual frame. The video frame rate is 30 frames per s and each frame consists of two fields of data made up of alternate intersecting lines on a screen which are scanned every $\frac{1}{60}$ s. For very fine time calculations, a single field could be captured and manipulated, but for our case it is sufficient to work with frames and time increments in multiples of $\frac{1}{30}$ s.

Our particular analysis method involves capturing five video frames, at known time intervals, that are some integer multiple of the time between frames ($\frac{1}{30}$ s), and then repeating this process at appropriately chosen time intervals of longer duration. This is analogous to the photographic 'snapshot' approach where a single picture of instantaneous velocities is produced at each particular time. Here we have the extra advantage of some error checking on the process. Since the $\frac{3}{4}$ inch VCR is programmable, we can automatically collect frames by counting the code from a particular mark on the tape and then digitizing the required picture as the tape plays. This method avoids noise errors that can be introduced when the VCR is manually paused to capture a picture to be digitized, a process that can cause a high level of random distortion. Using this 'capture-on-the-fly' method still introduces some random noise degradation at certain times, but with our equipment we found that by visually checking the digitized pictures and repeating the capture process for any badly degraded frames we could consistently capture well-resolved, relatively noise-free data.

Time series of data describing events of interest in the fluid motion were thus digitized and stored in either an IBM-PC or a Sun work-station for later data analysis.

In some cases we also captured the motion of selected particles over the total length of the experiment, i.e. A Lagrangian approach, in order to unravel the dynamics at the eastern end of the tank, in particular (see §4.1, figure 3).

3. Numerical techniques

Having stored the required data, we then proceed to retrieve, analyse and reduce it into a manageable form. The first step is picture enhancement and the identification of valid particle images within the captured frames. Having located the particles, we

N	Particle density	Bad matches	Velocity error (1 match)	Velocity error (2+matches)
361	8%	0	4.48%	1.36%
547	12%	0	4.43%	1.36%
716	15%	3	5.3%	3.7%

TABLE 1. Particle density (percentage of pixels containing particle images) against bad matches and velocity error for single and series (2+) matching tests

perform a centre-of-brightness calculation, which specifies the particle's image centre together with the average brightness of the pixels detected and the number of pixels above threshold for each particle. These values are stored as identifying parameters for future use in particle matching.

To perform this particle matching, we choose to define an energy function for the difference between the parameters of any two spot images in consecutively encoded frames. The form of this function E_{ij}, measuring the correlation between two particles i and j, is

$$E_{ij} = (x_i - x_j)^2 + (y_i - y_j)^2 + A(b_i - b_j)^2 + B(s_i - s_j)^2,$$

where (x_i, y_i, b_i, s_i) are the x-coordinate, y-coordinate, average brightness b and pixel size s respectively of the ith particle and the real constants A and B denote the relative importance of the brightness and size parameters in relation to the distance parameter, which for small displacements will obviously be the dominant matching parameter.

It should be realized that in spite of the many refinements adopted, there are still significant experimental discrepancies between two subsequent video frames. Sources of error include motion of the particles out of the light sheet, resulting in a large change in spot brightness and reduced chances of detection; noise and picture distortions in video recording and data transferral; and variations in the light-sheet intensity. All these factors increase the likelihood of particles being detected in one frame's data set but not in a subsequent one. The data 'drop-out' results in particle image data which cannot be matched, because the correct data record is missing. Errors of this type are unavoidable with the present scheme, but we can attempt to minimize them. Large particle velocities, inconsistent with those of their neighbours, are one indication that an erroneous match has taken place – we can prevent these errors by (*a*) limiting the distance over which a particle match is permitted and (*b*) compiling statistics of the particle matches in a specified region of the video frame and setting a velocity cut-off above which we assume an error has occurred.

To test the accuracy of the scheme when only two frames are involved, we use an artificial data set of spots whose density and velocity separation are determined. The test field is a horizontal shear with its centre at the mid-point of the frame. We use three different spot densities to test how closely particles can be placed, even to the point of overlapping in the most dense case, before an increase in error is found. Results for the three cases are given in table 1. The average error in velocities as a result of digitization error and the representation of a finite spot area by an integer number of pixels is found to be about 5% for the test case. If we use a time series of matchings as a criterion for a valid data point, then this error drops to 1.5% for the low-density cases and is only high (5%) for the dense case when a large number of erroneous matches are made. Allowing a time series of matches between data also eliminates many errors due to missing data.

When we have processed five frames in the time series to produce four sets of

matched velocity values, we perform the final automated error checking routine. Particle paths are scanned throughout the time sequence and only validated if the particle can be continuously traced through at least three frames. This eliminates single matches with a short time history and leaves only the data in which we have high confidence. As a final check, the velocity tracks are viewed on a monitor and obviously erroneous data which do not correspond with the observed video record are removed; this consists of perhaps 1 % of the data after all the automated data filtering has taken place.

The final process is the calibration of the data, translating the velocity values from pixel to physical coordinates using the reference grid coordinates, a process which removes any photographic-lens distortion in the data.

Velocities in the tank are now fully quantified and some of the results are shown in §4. To obtain desired flow quantities such as streamline patterns and vorticity values, further steps are needed. The first is to interpolate the velocity data onto a rectangular grid. Much debate concerning interpolation methods and the errors involved in the process exists in the literature. For a discussion, see Agui & Jimenez (1987) or Rignot & Spedding (1988), who describe some popular methods available and the error implicit in each method, found by a process known as 'bootstrapping'. After numerous tests, we find that the interpolation method which gives the lowest bootstrapping errors for our data is the Adaptive Gaussian Window (AGW). This is a correlation scheme in which errors are proportional to the local velocity fluctuations. The largest errors are found to be close to the sidewalls where friction generates a thin boundary layer (see figure 7). The particle tracking technique is unable to adequately resolve this region owing to the small lengthscale of the motion and the proximity of the nearby light-reflecting sidewall that degrades the particle contrast there.

Streamlines, vorticity and pressure fields are found by numerical integration of finite difference equations using the grid data as outlined in Imaichi & Ohmi (1983). For vorticity, there is a simple equation using just the velocity values, while evaluation of the pressure requires integrating the steady two-dimensional Navier–Stokes equations.

We also used the techniques described above to construct complete Lagrangian particle tracks during one entire experiment. An unbroken time series of frames was captured at time intervals small compared with the relative velocity-resolution timescale ((displacement lengthscale D)/(average ensemble velocity U)). Then the data were reduced using the LPIV method to derive particle displacements. Under the restriction that the particles remained in the light slice and within the bounds of the frame for the entire video record, we were able to follow particles throughout their entire motion and obtain detailed descriptions of particle excursions in the tank. Results using this technique will be presented in the following section.

4. Results

The flow in the whole tank was studied for several different changes in rotation speed, and some data were taken examining only the flow at the western end of the tank for very low and high Rossby numbers. For spin-up, we considered four cases and for spin-down two cases which were characterized by the Rossby number Ro defined as

$$Ro = \Delta\Omega/\Omega,$$

where $\Delta\Omega$ is the step change in rotation rate and Ω is the initial rotation rate.

We use the linear β-plane approximation to represent the northward change in Coriolis force with latitude on a sphere. This value is dependent on the mean depth

($\bar{h} = 12$ cm), slope of the bottom ($\alpha = \frac{1}{6}$), and the rotation rate ($\Omega = 0.07\ \mathrm{s}^{-1}$), all of which are the same for every experiment performed so β has a constant value of

$$\beta = 2\Omega\Delta h/\Delta y\bar{h} = 2\Omega\alpha/\bar{h} = 1.2 \times 10^{-2}.$$

At the same time, we can define a β Rossby number $U/\beta W^2$ as a measure of the ratio of inertial to Rossby wave timescales given by

$$Ro = \frac{\Delta\Omega}{\Omega}\frac{\bar{h}}{2W\alpha},$$

which is simply Ro times a geometric factor equal to 0.6 in the present case. Frictional effects must also be considered, the main effects coming from sidewall and bottom friction. The appropriate parameter is the Ekman number, E, which is constant throughout this work and is given by

$$E = \nu/2\Omega\bar{h}^2 = 2.5 \times 10^{-4}.$$

4.1 *The spin-up case*

As observed by van Heijst *et al.* (1990), the spin-up process for a *uniform-depth container* of arbitrary planform is characterized by three main stages: (*a*) an initial flow with $2\Delta\Omega$ relative vorticity; (*b*) flow separation at the tank corners and walls due to frictional boundary-layer effects, and the production of large vortices scaling with the tank dimensions (see also Monismith & Maxworthy 1989); and (*c*) organization of the flow into regular arrays of alternately cyclonic and anticyclonic vortices. Since we are dealing here with a β-plane flow, a preferred direction for the motion is established which leads to a break in the symmetry observed in those experiments.

The complete velocity time development of the spin-up case $Ro = 0.32$ is shown in figure 2 using data calculated with the LPIV method. At the impulsive start-up time, the main body of the flow performs anticyclonic geostrophic motion with constant initial vorticity ($2\Delta\Omega$). The no-slip condition on the sidewalls creates a thin boundary layer which grows slowly with time along all the walls of the tank. The flow in the eastern end of the tank rapidly slows, with motion decaying to a small magnitude relative to the rest of the tank. This end of the tank has effectively spun up within about the inertial timescale ($T_i = \pi\Omega^{-1} = 45$ s) (figure 2*b*) due to a mechanism that combines inertial and vortex stretching effects (see below). Since this end of the tank has rapidly reached a state of centrifugally balanced equilibrium at the new higher rotation rate, it follows that the free-surface height will be slightly greater at this end relative to its pre-adjustment value. A pressure gradient is then available to drive boundary wall jets against the main flow. As the counter-flow jet along the south (shallow) wall penetrates toward the west, it enters a region of adverse pressure gradient (or becomes unstable) and separates from the wall forming a large cyclonic vortex (figure 2*c*, *d*). This then propagates toward the west (figure 2 *e*) and helps intensify the western-wall boundary flow. Further vortex generation follows behind the initial vortex and these all propagate westward in sequence at approximately the Rossby wave speed for waves of this wavelength (taken as the distance between vortices, ~ 50 cm). A secondary feature has been developing in the north–west corner (figure 2*b et sequ.*) during this time. It is due apparently to boundary-layer separation in the corner (cf. Monismith & Maxworthy 1989 and van Heijst *et al.* 1990). Ultimately this vortex interacts with the first of the sequence of vortices propagating down the wall, causing it to propagate slowly eastward and into the interior (figure 2 *g*, *h*) by which stage the inertial flow is weak. The final approach to solid-body motion is completed by viscous dissipation in

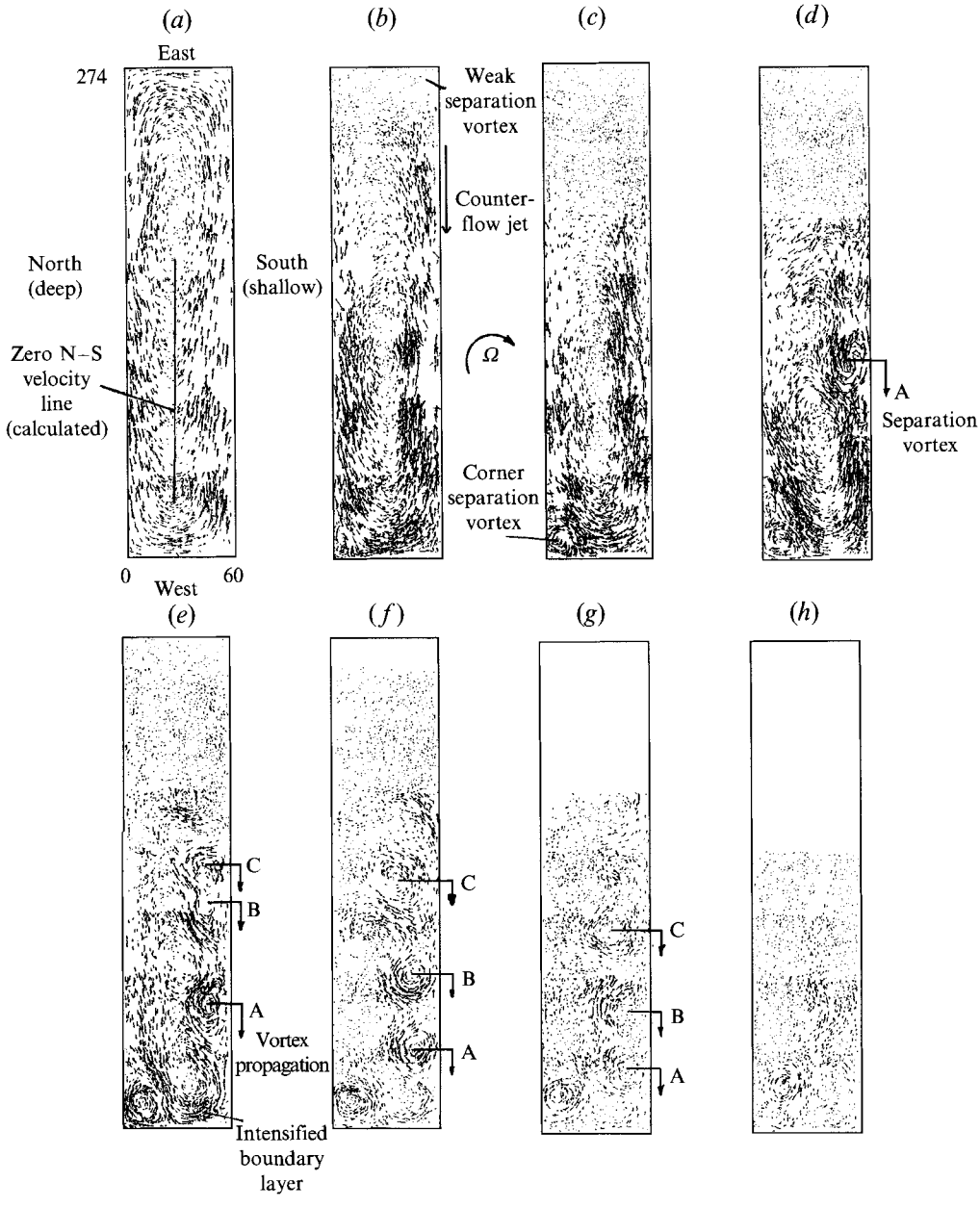

FIGURE 2. Instantaneous velocities for the spin-up case $Ro = 0.32$ at times: (*a*) $t = 5$, (*b*) $t = 30$, (*c*) $t = 45$, (*d*) $t = 60$, (*e*) $t = 90$, (*f*) $t = 150$, (*g*) $t = 210$ and (*h*) $t = 300$ s. A, B and C indicate locations of vortices formed by boundary-layer separation or instability. For clarity we indicate the locations of the shallow and deep sides of the tank as well as the corresponding geographical directions.

bottom Ekman and sidewall boundary layers on timescales much shorter than both the viscous-decay timescale $\bar{h}^2/\nu$ (~ 4 h) and the classical spin-up time in a rotating fluid with a free surface $2\bar{h}/(\nu\Omega)^{\frac{1}{2}}$ (~ 900 s).

Next we look more closely at the mechanisms that produce the rapid spin-up of the eastern end and the intensification of flow at the western boundary. The behaviour can be explained almost entirely in terms of the generation of relative vorticity by the initial spin-up flow field, i.e. the conservation of potential vorticity. Since the fluid is at rest

before start-up, the fluid initially has zero relative vorticity. After start-up, a relative anticyclonic vorticity equal to $2\Delta\Omega$ is generated everywhere in the tank so that the displacement of the centre of the resultant east–west shear flow can be calculated as follows. Assume that in the central portion of the tank and away from the curved flow at both ends the velocity profile is given by $U_0 - 2\Delta\Omega y$, where U_0 is the velocity at the shallow wall and y is the coordinate perpendicular to this wall. With depth given by $h_0 + \alpha y$, where h_0 is the depth at the shallow wall and α is the bottom slope, the condition that the net volume flux across any north–south section is zero gives

$$U_0 = \frac{2\Delta\Omega W[\frac{1}{3}\alpha L + \frac{1}{2}h_0]}{h_0 + \frac{1}{2}\alpha L}.$$

Thus the location of the plane of zero east–west velocity is given by

$$y_0 = \frac{W[\frac{1}{3}\alpha L + \frac{1}{2}h_0]}{\frac{1}{2}\alpha L + h_0}.$$

The location of this line of zero east–west velocity is shown in figure 2 for the spin-up case and figure 8 for the spin-down case. We see good agreement between its position and the location where particles are moving solely in the north–south direction. As a result of this initial motion with constant vorticity, a potential vorticity distribution of magnitude $(2\Delta\Omega)/h_0 + \alpha y)$ is set up.

Fluid close to the deep (northern) sidewall will move along lines of constant depth toward the western endwall. Here, as a result of tank topology, the flow must deflect across lines of constant depth from deep to shallow. As a consequence of potential vorticity conservation and the Taylor–Proudman theorem, columns of fluid in this flow will behave in a more-or-less two-dimensional manner and will decrease in length owing to movement up the shoaling slope. This will induce more anticyclonic vorticity into the columns than they already possess, so that they accelerate as they work up the slope. The flow nearer the eastern boundary can be explained in a similar way except that the vorticity generated by moving down the depth gradient generates cyclonic vorticity which rapidly cancels the anticyclonic vorticity the particles already possess. This accounts for the rapid spin-up of the fluid in the eastern third of the tank, followed by an inertial oscillation of the flow due to the relatively large value of *Ro* considered here. The scale of the observed fluid motion rapidly decreases to below that of the particle-separation resolution scale of the experimental technique (see figure 2*c*), even though they are still visible to the naked eye.

We can examine the trajectories of flow in the eastern end (see figure 3) to substantiate some of these arguments that are, in fact, applicable at either end. The trajectories shown are tracked continuously from $t = 0$ to 120 s with marks added to the paths at 30 s increments. From $t = 0$ to 30 s the motion is essentially inertial. Fluid columns moving down the gradient acquire cyclonic vorticity in order to satisfy potential vorticity conservation. Thus, theoretically, there is a final equilibrium latitude y_2 for each fluid column whose starting latitude y_1 is known. This position is given by

$$y_2 = y_1 + \Delta y = y_1 + \frac{\Delta\Omega}{\Omega}(h_0/\alpha + y_1),$$

where Δy is the displacement of the particle from its initial position y_1. In figure 3 we have marked the final position for the particles A–D and note that the agreement between the prediction is excellent except for B. Apparently particle E became trapped in a viscous corner flow during its overshoot phase while F was at an initial location

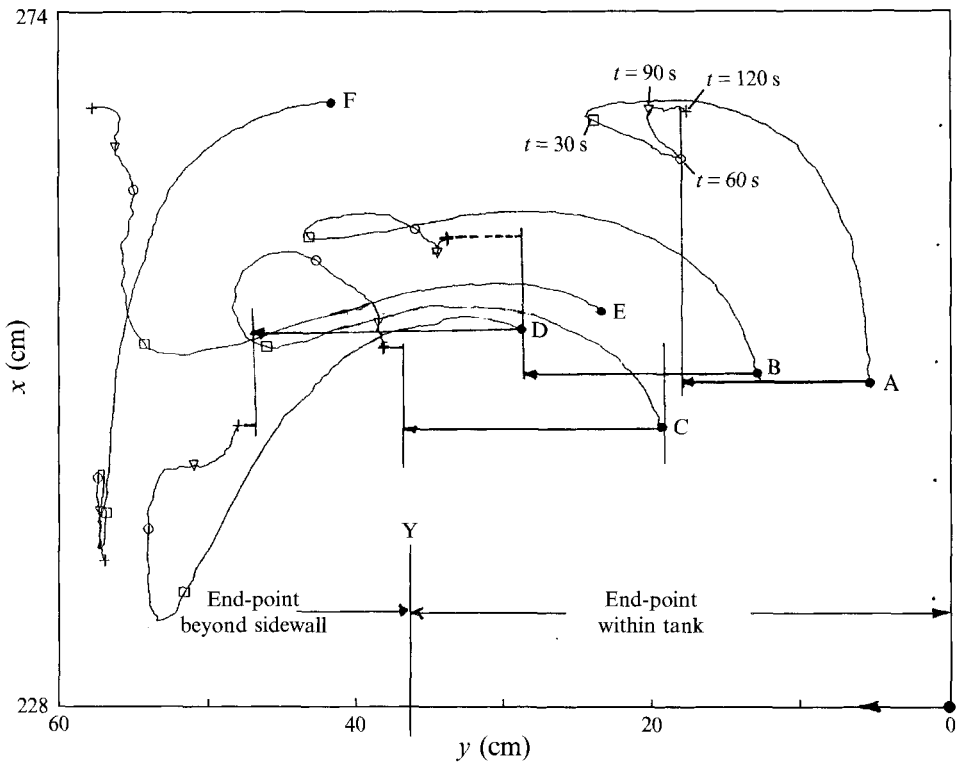

FIGURE 3. Continuous particle tracks for the times $t = 0$ to 120 s for the spin-up case $Ro = 0.32$ in the eastern end: □, $t = 30$; ○, $t = 60$; ▽, $t = 90$; +, $t = 120$ s. The line Y represents the initial position of particles that just touch the sidewall for the inviscid model. The final positions of the particles are noted according to vorticity-conservation concepts.

that would have brought it into contact with the sidewall. The sizable inertial motion at such large values of Ro moves the particles beyond their equilibrium position so that they have an excess of relative cyclonic vorticity with respect to their surroundings. Now the vorticity generation mechanism works in reverse and columns will move back up the gradient to lose excess vorticity and continue to oscillate until they spin down via the bottom Ekman boundary layer.

Thus the bulk of the fluid in the eastern end of the tank spins up very rapidly by a process that does not rely on viscosity in a time Δt_i of order $\Delta y/U_0$ given by

$$\Omega \Delta t_i = \left[\frac{3h_0}{\alpha W}\right]\left[\frac{2h_0+\alpha W}{3h_0+2\alpha W}\right] \approx 0.7 \quad \text{or} \quad \frac{\Delta t_i}{T_i} \approx 0.22$$

for the present case. For the case shown in figure 2, this time Δt_i is of order 10 s and its estimation has assumed that the particles move directly south–north at the largest possible velocity. From figure 3, we see that this can only be true for those particles very close to the eastern wall. The paths taken by the observed particles that start further out are curved and longer than those assumed in this calculation. Thus particle A traverses a path that is approximately 3 times longer than the direct route to its final location and it takes a time that is also approximately 3 times longer than that calculated crudely from the equation for Δt_i! Also based on these arguments, one would expect that there would be an orderly, spatial progression in the spin-up with particles closer to the eastern endwall reaching their rest positions before those further

out. This tendency is observed in figures 2(*b*) and 2(*c*), where the particles within 30 cm of the wall in figure 2(*b*) have effectively spun up by 30 s while particles within 80 cm in figure 2(*c*) take 60 s to spin up. At later times, this process can only extend slightly further westward, since a glance at figure 2(*a*) shows that it is only in this region that particles are being forced to move across the slope by the endwall constraint.

At this stage we must consider the further effects of friction on the flow. After $t \approx$ 30 s, the motion has formed observable frictional boundary layers of order 1 cm thick along all of the tank walls and a weak separation vortex in the southeastern corner (figure 2*b*). As a result of the rapid establishment of a high-pressure region at the eastern end (see figure 4*a*), boundary-layer fluid is forced to move westward along the shallow sidewall against the inertial flow. This return jet is very thin and is not detected when it first forms at about $t \approx 30$ s since there are no identifiable particles moving under its influence at this time (although the flow is visible to the naked eye as the movement of surface dust particles). However by $t \approx 45$ s (figure 2*c*) this return jet is carrying a thin stream of particles so that we can now resolve its velocity, but not its spatial structure. Return-jet velocity values are comparable to those in the inertial stream (4–5 cm s^{-1}) but of the opposite sign. Thus it is in the form of a thin wall jet on the outer edge of which is established a very large cyclonic vorticity. Initially the return jet accelerates as it moves westward but a time is soon reached when it separates owing to the adverse pressure gradient at that location (see figure 4). This causes the formation of a recirculating cyclonic vortex which then breaks away from the boundary layer and is thrust into the inertial flow (figure 2*c*, *d*). This vortex then propagates westward due to its self-induction, i.e. motion induced because of its proximity to the wall. Thereafter more vortices form to the east of the original one. This train of vortices continues to move westward, interacting with the inertial anticyclonic outer flow to generate alternating cyclones and anticyclones along the southern wall. These westward-moving vortices, or waves, eventually compress the anticyclonic flow along the western wall into an intense inertial boundary layer flow (figure 2*e*).

One can also interpret these propagating vortices as Rossby waves since their velocity scales are comparable to the Rossby wave propagation speed (0.3–0.5 cm s^{-1}) toward the western end (see figure 2*f*). The characteristic lengths of the vortices are also shown to scale with the Rossby deformation radius – each vortex is approximately 20 cm in size, which is comparable to $(U/\beta)^{\frac{1}{2}}$.

Thus, between $t \approx 60$ and ≈ 90 s, a train of alternating cyclonic and anticyclonic vortices is generated which transfers energy from the largest basin scale to small scales and this marks the start of the final stages of spin-up by viscous dissipation. The southern sidewall vortices continue propagating toward the western end and decay with time. During most of this time, the single cyclonic vortex that was being formed by boundary-layer separation in the north-western corner has grown to about the same size as the southern sidewall vortices. This vortex deflects the wall current on the north or deep-side so that it crosses the depth gradient more obliquely. In the process, the original inertial flow in the southwestern corner is dominated by the presence of the two converging cyclonic vortices. The anticyclonic flow is forced into the corner where its energy is dissipated rapidly, presumably by bottom boundary-layer and wall-friction effects. By $t \approx 300$ s (figure 2*h*), the motion has decayed to such an extent that the dominant scales are smaller than the particle resolution lengthscales and the flow can no longer be effectively tracked by our method.

Overall the domain-averaged velocities decay exponentially and the decay rate can be found by plotting the logarithm of the average absolute velocity (taken as the root-

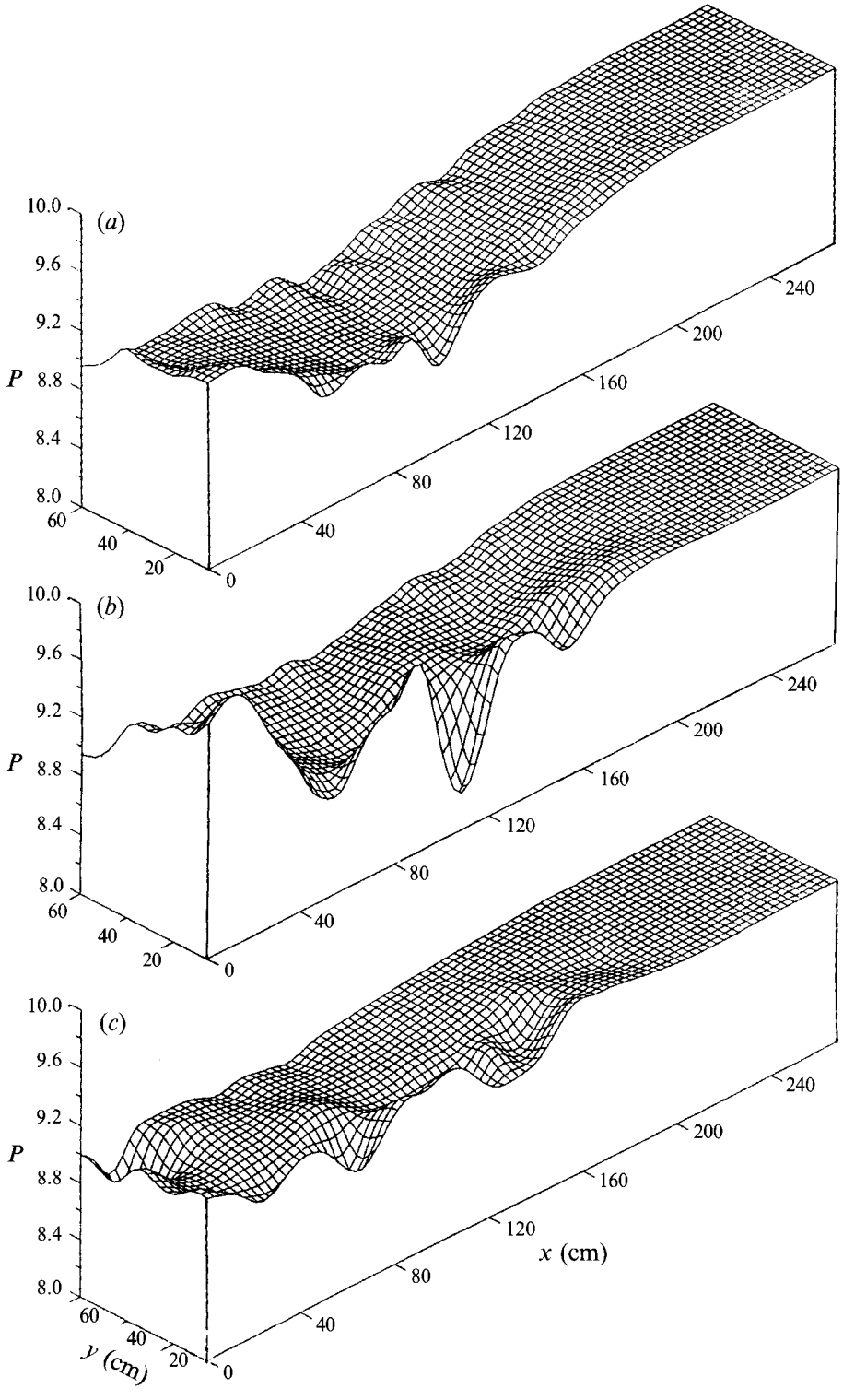

FIGURE 4. Pressure relief maps at times (*a*) $t = 45$, (*b*) $t = 60$ and (*c*) $t = 90$ s.

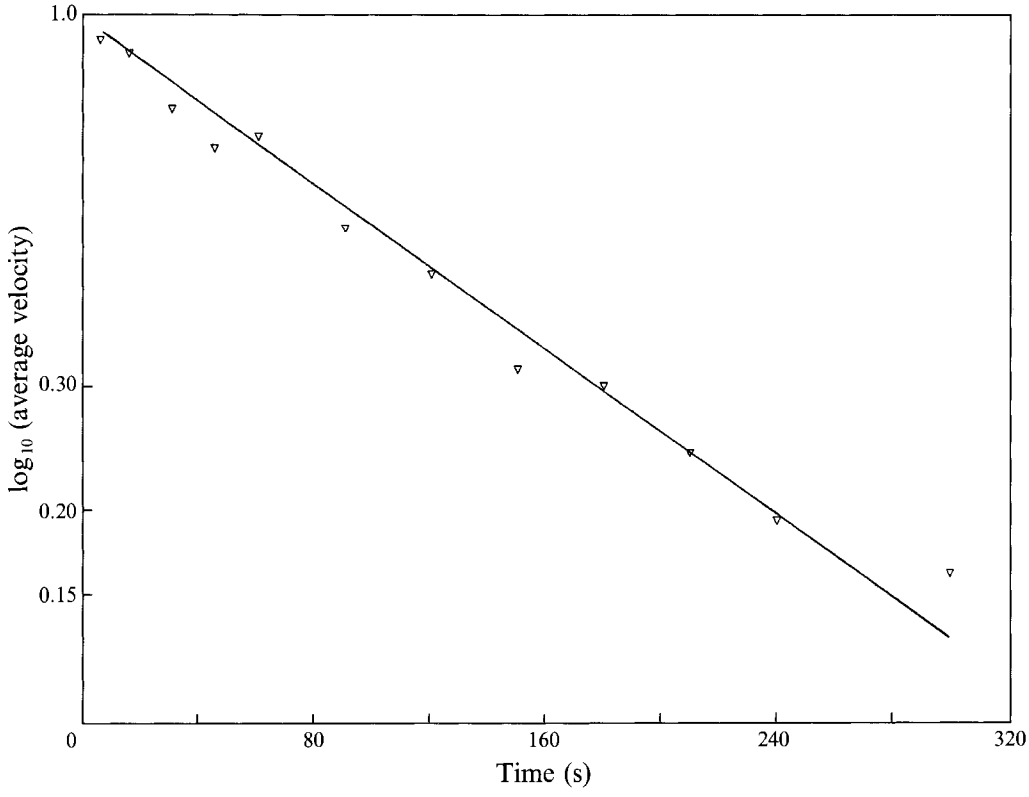

FIGURE 5. Log-linear plot of absolute velocity, averaged throughout the whole tank, verses time, for the spin up case $Ro = 0.32$.

mean-square average of all particle velocities in the tank) against time (see figure 5). For this case, the e-folding spin-up time is 143 s which is to be compared to the 'classical' spin-up time for a flat-bottomed container with a free surface, which is $T_c = 2\bar{h}/(\nu\Omega)^{\frac{1}{2}} \approx 900$ s. We note that van Heijst's experiments have shown that T_c is the relevant timescale even for non-circular geometries with a flat bottom, and thus the inclusion of a β-effect has had a dramatic influence on the spin-up time. At times after 300 s, the resolution of the particle tracking error becomes significant compared to the flow velocities, as can be seen from the deviation from exponential spin-up observed at large times in figure 5.

For completeness, we show the vorticity in figure 6 at moderately early times, and this reinforces the statements made above concerning the vortex generation process along the southern wall in particular. Maximum bootstrap errors in vorticity of the order of 10% can be associated with regions close to the sidewalls where resolution is the poorest (see figure 7). Average velocity errors for different concentrations of particles in a test case are given in table 1. We assume pressure errors will be of a similar magnitude since pressure values are calculated from the Navier–Stokes equation which involves an integration over velocity and velocity gradients.

We have also examined the sequence that takes place for spin-up cases with smaller values of the Rossby number. It is found that for the reduced initial velocities generated in these cases, the vorticity cancellation mechanism described earlier is more effective and flow in the easternmost section is damped more quickly since there is now no overshoot in the decay to equilibrium. Values of the exponential decay rate of velocity,

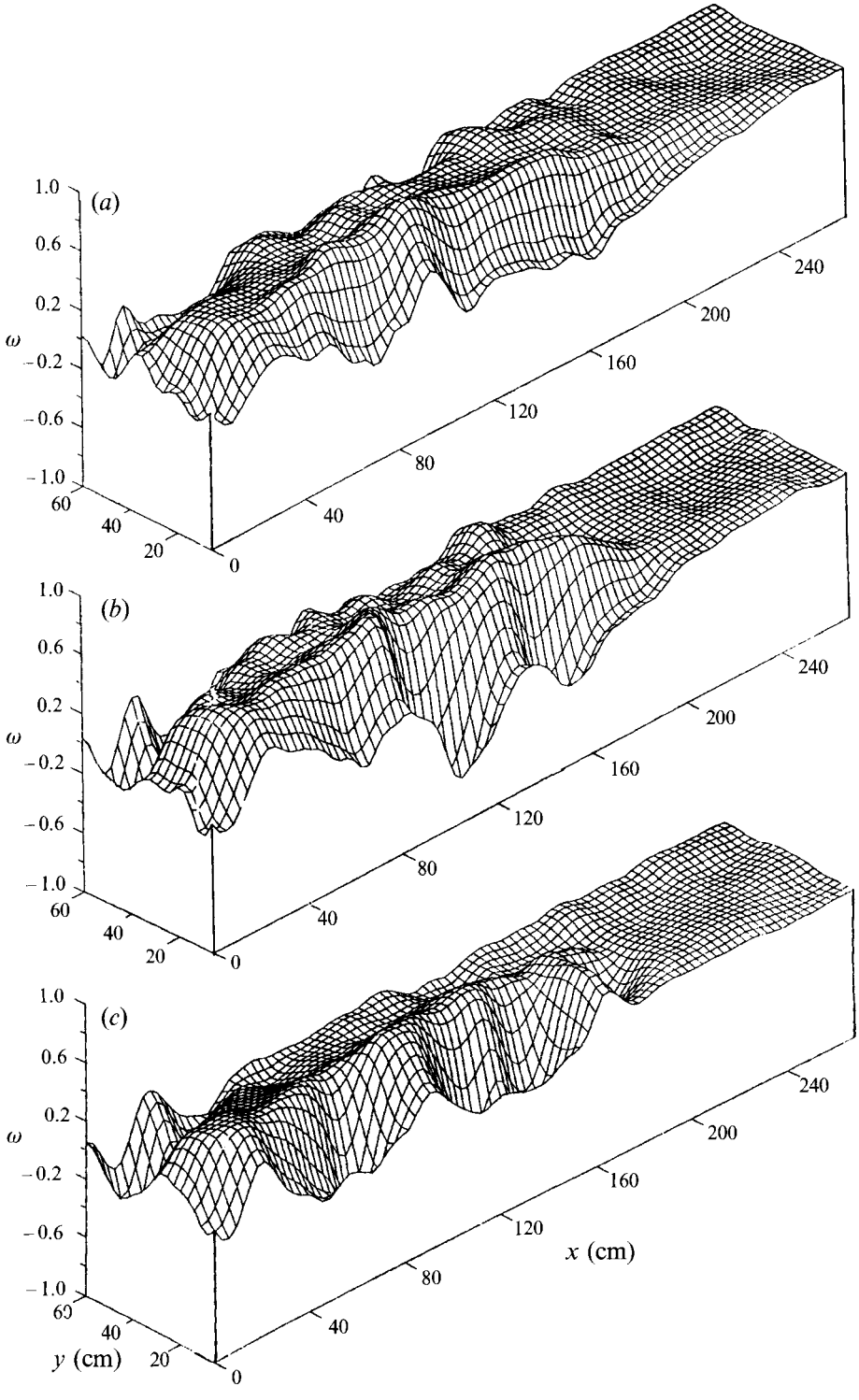

FIGURE 6. Vorticity relief maps at times (*a*) $t = 45$, (*b*) $t = 60$, and (*c*) $t = 90$ s.

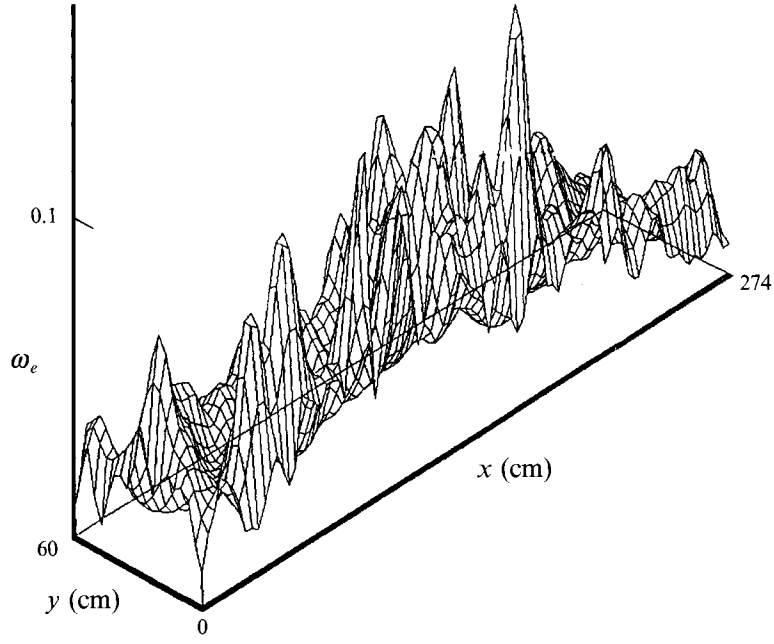

FIGURE 7. Relief plot showing absolute vorticity bootstrap error (given as a decimal fraction of the absolute vorticity) at time $t = 5$ s throughout the whole tank.

(*a*)	*Ro*	γ	T_s	T_s(flat)	(*b*)	*Ro*	γ	T_s	T_s(flat)
	0.06	0.0061	164	900		0.20	0.0076	132	900
	0.11	0.0062	161	900		0.32	0.0062	161	900
	0.20	0.0076	132	900					
	0.32	0.0068	147	900					

TABLE 2. (*a*) Domain-averaged velocity decay rate (γ) and spin-up time T_s versus *Ro* for the spin-up cases. T_s (flat) is the theoretically predicted spin-up term for a flat-bottomed container of the same depth as the average depth in the present case. (*b*) As (*a*) but for the spin-down case.

γ, against Rossby number are given in table 2(*a*) where $|v(t)| = v(0)\,e^{-\gamma t}$. Interestingly the spin-up time is not much affected by variations in *Ro* and is three to four times larger than the inertial timescale ($\pi/\Omega = 45$ s). Since the eastern end spins up within this latter timescale, it appears that the overall dynamics is dominated by the events that take place in the western end of the tank. For $Ro = 0.2$, only two vortices are formed between the shallow endwall and the western sidewall by $t \approx 60$ s, and the vortex strength is much weaker. For very small Rossby number, $Ro = 0.06$, the whole tank, apart from the western end, is spun up within the inertial timescale, so that the only motion on a scale large enough to be observed is a stream moving up the bottom slope at the western end and the production of a weak vortex close to the western wall.

4.2 *The spin-down case*

Because of the asymmetry introduced by the sloping tank bottom, we can anticipate that the spin-down case will be qualitatively different from the spin-up case, and this is indeed found to be true at later times but not initially. At start-up, instead of increasing the tank rotation speed we decrease it so that the inertial start-up flow moves

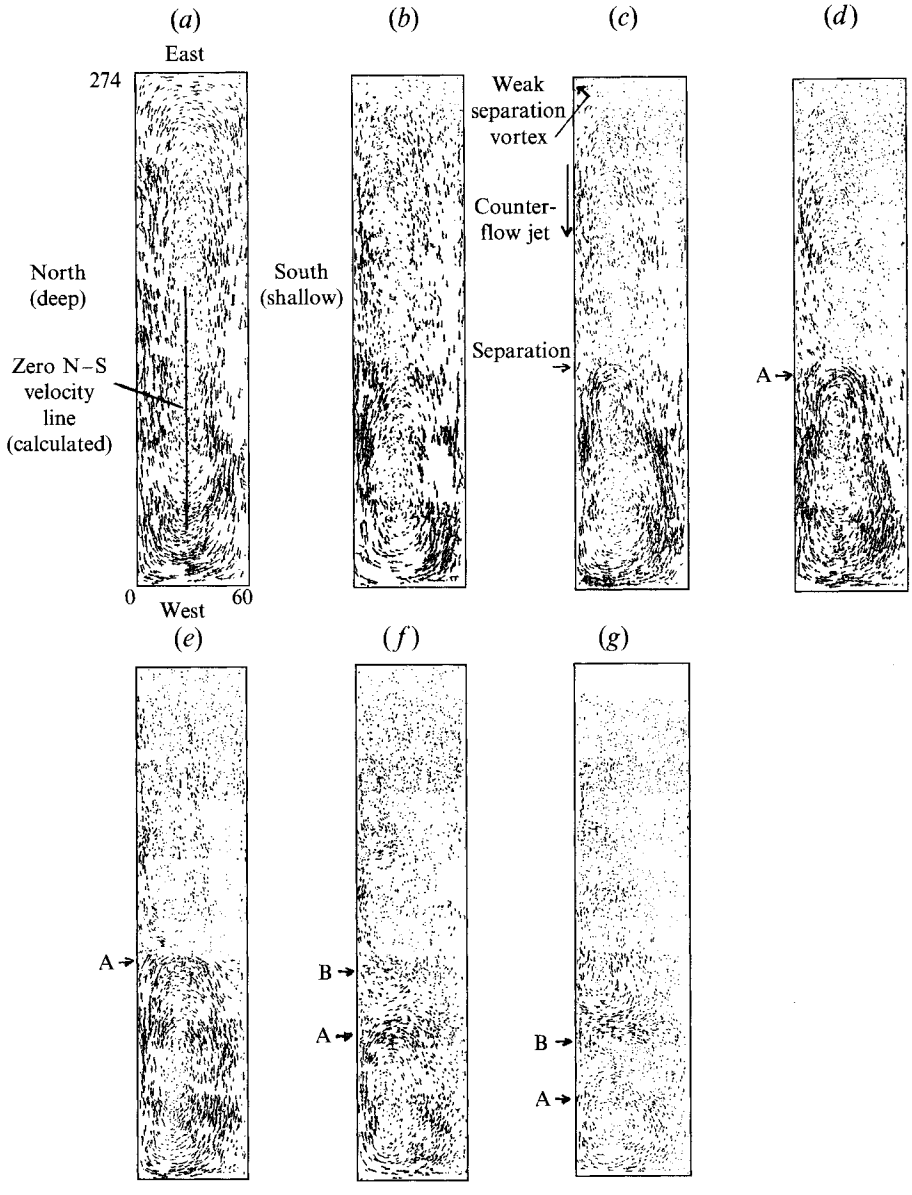

FIGURE 8. Instantaneous velocities for the spin-down case $Ro = 0.32$ at times: (*a*) $t = 5$, (*b*) $t = 30$, (*c*) $t = 45$, (*d*) $t = 60$, (*e*) $t = 90$, (*f*) $t = 150$, and (*g*) $t = 210$ s. A and B indicate the locations of boundary-layer separation.

in the opposite direction to that observed previously (see figure 8*a*). The initial flow relative to the spun-down container is thus clockwise, i.e. cyclonic relative vorticity of value $2\Delta\Omega$ is generated. Consideration of some of the mechanisms characterizing the spin-up flow still hold in this case. We consider a spin-down case of the same magnitude as that described for spin-up, i.e. $Ro = 0.32$. At the eastern end fluid moves up the gradient so that anticyclonic vorticity is generated by fluid columns as they conserve potential vorticity. Thus the damping mechanism with topographically induced anticyclonic vorticity cancelling pre-existing cyclonic vorticity functions in exactly the same way as previously but with the velocity direction reversed. As before

the high pressure generated in the eastern half of the tank will interact with both a weak separated vortex in the north-east corner and the boundary layer on the deep wall to induce a flow toward the western end counter to the inertial motion. Again, flow separation (or instability) causes the westward-flowing jet to be deflected into the middle of the tank, as shown in figure 8*c*, *d*.

At the western end, the enhanced cyclonic vorticity generated by flow down the slope generates a jet moving eastward along the deep wall (see figure 8*b*). About halfway down the tank, this jet separates from the wall as it interacts with the counter-flowing wall jet from the eastern end discussed above. A large, cross-tank jet is formed which effectively bisects the tank as seen in figure 8*c*, *d*). Flow in the tank is then separated into two distinct circulation patterns, a steady weak eastern-end circulation and a persistent western-end circulation with some small amount of fluid possibly being exchanged between the two systems. The centre of the western-most, intense vortex is slowly displaced westward, as a Rossby wave, intensifying the inertial boundary layer at the western wall and enhancing dissipation there. Ultimately it breaks into three vortices (figure 8*e*, *f*), presumably as anticyclonic vorticity is injected into the flow from the separated boundary layer. Both circulations are cyclonic while the vortex in the middle of the tank is anticyclonic.

We note here similarity to a largely overlooked paper by Pedlosky (1965) in which an analytical model of an ocean basin in which an oscillatory wind stress with zero mean drives an unsteady flow. While the mathematical detail behind this is interesting, more important to our application is the description of the resultant flow. For a resonant case the flow splits into a rapidly flowing western basin circulation and a decreasing eastern flow as in the case presented here.

For smaller values of the Rossby number, the western-end circulation is initially enclosed in a much reduced area and the large 'mid-tank' vortex forms closer to the western endwall. The decay rates for exponential reduction in relative velocity for the spin-down cases can be found in table 2(*b*). Here, as in the spin-up case, the spin-down time is of the order of 150 s and is insensitive to changes in *Ro*, again demonstrating the dominant effect the topographic β-effect has on the development of the fluid motion.

5. Discussion

Comparing the present method of particle tracking to others that are currently available, we find that we can obtain a much greater control of the estimate of the error and eliminate the human inaccuracies involved in the hand digitizing of data, while the cost of implementing the technique is a fraction of that required for fully functional laser-Doppler equipment, for example. Tests performed upon other data sets, with very high particle concentrations, show that the scheme still can accurately resolve velocity fields, even when the particle images are so dense that they overlap.

One obvious prior example with which we can compare our results is that due to van Heijst *et al.* (1990), who considered spin-up in a flat-bottomed rectangular container of aspect ratio $L/W = 3$. In that case an initial motion of constant vorticity $2\Delta\Omega$ was followed by separation of vortices in the two corners into which the flow along the long sides of the tank was moving. These separation vortices grew and induced further separation vortices until the tank was eventually filled with counter-rotating vortices that were more-or-less circular and spanned the width of the tank. These vortices then decreased by the conventional Ekman-layer pumping mechanism. In the present case, this scenario is greatly modified. The start of spin-up/down produces an initial flow of

constant relative vorticity but non-constant potential vorticity. Separation again occurs in the same two corners (dependent on initial flow direction) but, before it can evolve, the pressure gradient generated by the rapid spin-up of fluid at the eastern end has generated a counterflow wall jet that, within one rotation period, penetrates westward. In the spin-up case, this jet separates from the wall or becomes unstable to generate a sequence of smaller-scale vortices that propagate slowly westward. The vortices do not extend beyond the tank centreline. Eventually the leading one intersects with the western endwall and impinges upon the separation vortex that has been growing there. At this stage, the overall flow strongly resembles a number of the analytical/numerical models that have been proposed for the basin-scale motions of the world's oceans. Here, as in the case considered by Moore (1963) with $Re \gg 1$, it is not possible to generate sufficient dissipation in the western boundary current to balance the energy input. It becomes necessary for the flow to develop a wavy structure on the southern wall (in this case) to account for the increased dissipation and energy radiation needed to balance the energy input in the steady case and the spin-up of fluid in our case. In our case, $Re \sim O(10^4)$ and so we observe the types of structure calculated by Moore (1963).

The spin-down case has some similarities in that separation vortices form in the opposite two corners, one of which generates a counter-flowing wall jet. When the latter interacts with the main flow, however, it forms a large anticyclonic vortex in the tank centre that ultimately spans the tank width. This structure propagates westward and the flow eventually breaks up into several counter-rotating vortices. The pattern, however, is not as well-defined as in the spin-up case.

While completing this paper, the authors became aware of work being done with a very similar objective by Maas *et al.* (1992). A rectangular tank with a small aspect ratio ($L/W \sim 0.5$) was used there. As a result, the east–west flow was dominated by the close proximity of the east and west walls, resulting in a flow evolution rather different from that observed here. In particular, they explain some of their results by invoking three dimensional, i.e. non-hydrostatic, effects that are clearly less important in our case. Also the kind of repeatable, organized vortical structures that evolve in our case appear to be missing in their experiments, although at present we do not have sufficient detail to make a complete comparison.

The authors would like to thank Dr F. Browand for invaluable discussions and Dr G. Spedding for help in coming to terms with many different hardware systems. The suggestions of the referees for improvements are greatly appreciated. We thank, also, Dr R. C. Beardsley for a careful reading and correction of the manuscript. Support is acknowledged for the Office of Naval Research with funding from grant numbers N00014-86-K-0679 and N00014-89-J-1400.

REFERENCES

AGUI, J. C. & JIMENEZ, J. 1987 On the performance of particle tracking. *J. Fluid Mech.* **185**, 447–468.

BEARDSLEY, R. C. 1969 A laboratory model of the wind-driven ocean circulation. *J. Fluid Mech.* **38**, 255–271.

BEARDSLEY, R. C. 1975*a* The 'sliced cylinder' laboratory model of the wind-driven ocean circulation. Part 1. Steady forcing and topographic Rossby wave instabilities. *J. Fluid Mech.* **69**, 27–40.

BEARDSLEY, R. C. 1975*b* The 'sliced cylinder' laboratory model of the wind-driven ocean circulation. Part 2. Oscillatory forcing and Rossby wave resonance. *J. Fluid Mech.* **69**, 41–64.

BENTON, E. R. & CLARK, A. 1974 Spin-up. *Ann. Rev. Fluid Mech.* **6**, 257–280.

BRYAN, K. 1963 A numerical investigation of a non-linear model of a wind-driven ocean. *J. Atmos. Sci.* **20**, 594.

FOFONOFF, F. 1954 Steady flow in a frictionless, homogeneous ocean. *J. Mar. Res.* **13**, 254–262.

GREENSPAN, H. P. 1968 *Theory of Rotating Fluids.* Cambridge University Press.

HEIJST, G. J. F. VAN. 1989 Spin-up phenomena in non-axisymmetric containers. *J. Fluid Mech.* **206**, 171–191.

HEIJST, G. J. F. VAN, DAVIES, P. A. & DAVIS, R. G. 1990 Spin-up in a rectangular container. *Phys. Fluids* A **2**, 150–159.

IMAICHI, K. & OHMI, K. 1983 Numerical processing of flow-visualization pictures-measurement of two-dimensional vortex flows. *J. Fluid Mech.* **129**, 283–311.

MAAS, L. R. M., HEIJST, G. J. F. VAN & WILLIAMS, C. W. M. 1992 The Spin-Up of fluid in a rectangular container with a sloping bottom. *AGU-Ocean Sciences Conf. Abstract. New Orleans, Louisiana January 27–31, 1992.*

MOORE, D. W. 1963 Rossby waves in ocean circulation. *Deep Sea Res.* **10**, 20–27.

MONISMITH, S. G. & MAXWORTHY, T. 1989 Selective withdrawal and spin-up of a rotating stratified fluid. *J. Fluid Mech.* **199**, 377–401.

PEDLOSKY, J. 1965 A study of the time dependent ocean circulation. *J. Atmos. Sci.* **22**, 267–272.

PEDLOSKY, J. 1979 *Geophysical Fluid Dynamics.* Springer.

PEDLOSKY, J. & GREENSPAN, H. P. 1967 A simple laboratory model for oceanic circulation. *J. Fluid Mech.* **27**, 291–304.

RIGNOT, E. J. M. & SPEDDING, G. R. 1988 Performance analysis of automated image processing and grid interpolation techniques for fluid flows. *USC Aerospace Engineering Rep.* USCAE 143.

STOMMEL, H. 1948 The westward intensification of wind-driven ocean currents. *Trans. Am. Geophys. Union* **29**, 202–206.

VERONIS, G. 1966 An analysis of wind-driven ocean circulations with a limited number of Fourier components. *J. Atmos. Sci.* **20**, 577–593.